Case Studies in Construction Materials 18 (2023) e02077

Contents lists available at ScienceDirect

Case Studies in Construction Materials

journal homepage: www.elsevier.com/locate/cscm

Numerical aspects of phase field models for low-temperature fracture in asphalt mixtures

Awais Ahmed [a], Javed Iqbal [b], Sayed M. Eldin [c], Rawid Khan [b], Mudassir Iqbal [b,*]

[a] Department of Built Environment, Oslo Metropolitan University, 0166 Oslo, Norway
[b] Department of Civil Engineering, University of Engineering & Technology, 25000 Peshawar, Pakistan
[c] Center of Research, Faculty of Engineering, Future University in Egypt, 11835 New Cairo, Egypt

ARTICLE INFO

Keywords:
Finite element method
Phase field model
Cohesive zone model
Quasi-brittle fracture
Asphalt concrete

ABSTRACT

Unlike the cohesive interface element model, the phase field model (PFM) is a newly developed computational model which provides a unified approach to predicting crack nucleation, propagation, coalescence and branching without any ad-hoc criterion. Over the years, several variants of the phase field model are presented. This paper aims to investigate the suitability of different phase field models and determine the optimal characteristic functions/model parameters for low-temperature fracture in asphalt mixtures. The analysis results of the phase field method (which belongs to a class of diffuse damage models) are also compared with the interface element model (which belongs to a class of discrete damage models). The models are compared by examining the governing equations and performing numerical simulations on single-edge notch specimens. Furthermore, various aspects of cohesive zone model (CZM) based PFM are discussed including the type of softening laws and damage growth under uniform/non-uniform stress states. It is concluded that brittle phase field models are not fully capable to predict fracture in asphalt mixtures even at low temperatures.

1. Introduction

Cohesive zone model (CZM) with interface elements is often used to simulate damage in asphalt mixtures. Over the years several researchers successfully simulated damage in asphalt mixtures under mechanical and/or thermal loads at the meso/micro-structural level using cohesive interface elements. In the interface element model, the interface elements are inserted along the finite element boundaries to simulate cracking. A nonlinear cohesive constitutive law, in addition to the bulk constitutive law, is used to simulate material nonlinear behavior ahead of crack tip. One of the pioneering works in damage modelling of asphalt mixtures using interface elements is by [1]. [1] used cohesive elements on a predefined crack path to simulate mode-I fracture in an indirect tension test (IDT) specimen. A cubic decaying function proposed by [2] was used to simulate nonlinear material behavior around crack tip. [3] used cohesive interface elements to simulate mode-I and mixed-mode fracture in asphalt concrete. A potential based cohesive constitutive law with an exponentially decaying function [4] was used to simulate nonlinear material behavior ahead of crack tip. [5] and [6] used a micro-mechanical approach to study the effect of material heterogeneity on fracture mechanisms of asphalt concrete. Mode-I and mixed-mode fracture tests were numerically simulated using discrete element method. A bi-linear cohesive constitutive law was used to simulate crack initiation and propagation. Numerical results of mode-I fracture showed good agreement with the experimental

* Corresponding author.
E-mail address: mudassiriqbal@uetpeshawar.edu.pk (M. Iqbal).

https://doi.org/10.1016/j.cscm.2023.e02077
Received 26 January 2023; Received in revised form 9 April 2023; Accepted 15 April 2023
Available online 28 April 2023

results, both qualitatively and quantitatively, whereas good qualitative results were obtained for mixed-mode fracture. [7] used a cohesive zone model to simulate rate dependent fracture in an asphalt mixture. A detailed finite element model, considering the microstructural details, was developed to study rate dependent fracture.

Several researchers have successfully used cohesive zone model with interface elements to simulate moisture induced damage in asphalt mixtures, see for example [8,9]. [8] proposed a micro-mechanical model for the simulation of moisture induced damage in asphalt mixtures. Cohesive zone elements were embedded in the finite element mesh to model effect of moisture on damage evolution. However, the direction of crack propagation was predefined in their simulations. Cohesive zone model was also used to simulate thermally induced reflective cracking in asphalt pavements [10,11]. [12] proposed a multiscale approach for the analysis of asphalt pavements. A multiscale thermo-mechanical finite element model was used to connect the heterogeneous local scale with the homogeneous global scale of asphalt pavements. Cohesive zone model was used to simulate damage evolution at the local scale.

A discrete damage model like the cohesive interface element model is a good choice to simulate fracture in solids, however, the cracks are only allowed to grow along finite element boundaries. Moreover, generation of a finite element mesh with interface elements sometimes becomes cumbersome. Therefore, diffuse damage models are often preferred, see for example [13–16]. Diffuse damage models simulates a sharp crack as a damage smeared over a finite volume. The resulting formulation does not require a special finite element mesh and the model can be easily implemented in a computer program. Moreover, diffuse damage models does not require an algorithm to explicitly track a crack path and is able to model multiple cracks and complex crack typologies.

Phase field method is a newly developed diffuse damage model which is based on the variational approach to brittle fracture. The damage is a natural outcome of an analysis obtained by the minimization of the total potential. Phase field model (PFM) simulates damage like diffuse damage models and therefore easy to implement but at the same time can simulate sharp cracks like interface element model and therefore does not suffer from mesh dependency problem. One of the advantages of phase field method is its generality. Owing to the variational structure, the phase field method is able to simulate complex cracking patterns and multi-physics problems [17–19] in a consistent manner with a relatively simple computer implementation. Moreover, extension to 3D problems is straightforward. Phase field method emerged from the pioneering work of [20]. They presented a variational formulation for brittle fracture where the total energy is minimized with respect to both displacement field and crack geometry. As a result, crack initiation, propagation and branching is taken into account in a single framework. Thereby, removing the limitation of Griffith's theory. However, this model suffers from the localization problem as the displacement field is discontinuous in the presence of cracks. [21] presented a regularized version of the phase field model by introducing a length scaling factor. As a result, the cracks are modelled as diffuse damage instead of sharp cracks. Moreover, a Dirichlet-type condition was applied to the damage phase field to ensure irreversibility of the cracking process during unloading. [22] and [23] presented a regularized phase field model for brittle fracture based on thermodynamic framework. The irreversibility of the damage phase field was ensured by satisfying the second law of thermodynamics (i.e. damage phase field is always positive and monotonically increasing). However, these models are limited to simulate brittle fracture. In order to simulate fracture in quasi-brittle materials [24] presented a phase field model employing the cohesive zone model. However, the method requires a crack path to be known a priori which undermines the good features of diffuse damage models. [25] presented a thermodynamically-consistent phase field model for modelling damage in quasi-brittle materials based on the concept of cohesive zone model. One of the key ingredients of phase models is the degradation function. The degradation function determines how the stored bulk energy evolves with changes in damage phase field. The degradation function used in most of the phase field models for brittle fracture, e.g [21,22,26,27] is not able to simulate quasi-brittle failure of material. Therefore, [25] presented a rational based degradation function whose parameters can be adjusted to reproduce the given softening behavior, e.g. linear softening, exponential softening etc., similar to the cohesive constitutive laws. The model is able to simulate complex crack typologies without any ad-hoc criterion. Noteworthy is the work of [28] and [29] who used a phase field model to simulate fracture in asphalt mixtures. Numerically obtained peak loads and qualitative comparison of crack paths showed good agreement with the experimental results. However, the authors [28,29] used a cubic degradation function which is more suitable to simulate brittle fracture [27]. Moreover, a double-well potential function was used to model the local fracture energy. The use of double-well potential function is not well suited for simulating fracture in solids and may give unrealistic damage patterns [27]. Therefore, monotonic crack geometric functions are often used in phase field models. [30] presented a phase field model for simulating quasi-brittle failure of asphalt mixtures. A monotonic crack geometric function with a rational based degradation function of [25] was used. The model successfully simulated mode-I and mixed mode fracture in asphalt mixtures.

Over the years several variants of phase field models are presented which raises questions like (i) which phase field model is more appropriate for damage modeling in asphalt mixtures? (ii) which phase field model functions are suitable for numerical simulation of asphalt mixtures (iii) what is the effect of different softening laws on structural response, damage profile and model performance when used in conjunction with phase field models? and (iv) what are differences and similarities between interface element and phase field model. Among variously available phase field models, i.e. brittle and quasi-brittle phase field fracture models, this paper aims to investigate the suitability and potential of these models for accurately simulating damage in asphalt mixtures. The literature is also devoid of comprehensive study on the effects of cohesive constitutive laws on damage growth using phase field model. Additionally, a comparative study of the cohesive zone model with interface elements and the cohesive zone model with phase field method is lacking in the literature. Therefore, it is the aim of the paper.

- to compare different phase field models for damage predictions in asphalt mixtures. Especially, the suitability of phase field models presented by [22] (brittle fracture PFM) and [25] (brittle/quasi-brittle PFM) is assessed for the simulation of damage in asphalt mixtures at low temperatures.
- to investigate the effect of type of softening laws on the performance of the phase field model and on structural response.

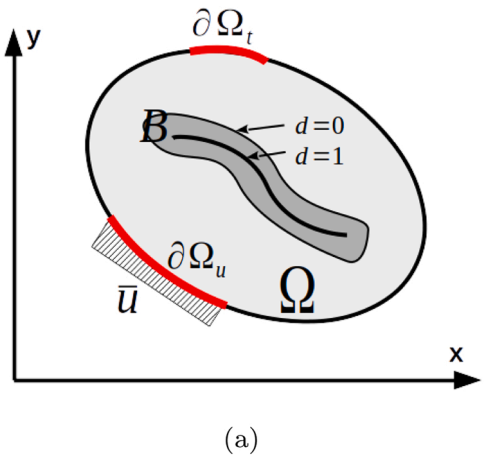

(a)

Fig. 1. A solid body with a diffuse crack.

- to investigate the effect of phase field model parameters on the response.
- to compare the interface element and phase field models in terms of damage prediction and model parameters.

It is further highlighted in the manuscript that only qualitative damage profiles and peak load calculations are not enough to correctly validate a numerical model, instead the post peak response is also necessary for model verification. The present contribution will be helpful in the selection of appropriate PFM characteristic functions and parameters for damage modeling in asphalt mixtures at low temperatures in future studies.

Remaining of the manuscript is organized as follows. Section 2 and 3 briefly describe the governing equations of phase field model and interface element model. The performance of different damage models is discussed using a numerical test on single edge notch beam specimen in section 4 followed by a parametric study to highlight the effects of phase field model parameters like the softening behavior, mesh size and length scaling factor. Concluding remarks are summarized in section 5.

Remark 1. The degradation function used in some of the phase field models [22,27,28] is closely related to the brittle fracture. These models mimic an elastic behavior of the material until peak load and quick loss of strength after the peak load. Moreover, the phase field model proposed by [22] is more commonly used phase field model. Therefore, it is selected as a representative phase field model to simulate brittle fracture. Note, that the phase field model proposed by [28] is not used due to the above mentioned drawbacks. Moreover, the degradation function used in [28] is closely connected to the brittle fracture models of [22,27], so one can expect that the similarities/differences related to brittle/quasi-brittle fracture pointed out in this paper also hold for the model in [28].

2. Phase field model

Consider a solid body with a domain Ω, Fig. 1. The body is subjected to prescribed displacements $\bar{\mathbf{u}}$ on the surface $\partial\Omega_u$ and prescribed tractions $\bar{\mathbf{t}}$ on the surface $\partial\Omega_t$. The body is also subjected to body forces $\bar{\mathbf{b}}$ and contains an internal surface/crack, S represented as a diffuse damage over the domain B. In addition to the displacement field $\mathbf{u}$, a damage phase field, d is defined in the domain Ω. The damage phase field d varies between 0 and 1 in the regularization band B such that $d = 0$ represents the intact solid and $d = 1$ represents fully damaged material. The spaces of displacement field ($\mathscr{U}_u$), damage phase field ($\mathscr{U}_d$) and their variations ($\mathscr{V}_u$, $\mathscr{V}_d$) are given as

$$\mathbf{u}(\mathbf{x}) \in \mathscr{U}_u := \{\mathbf{u} | \mathbf{u}(\mathbf{x}) = \bar{\mathbf{u}}\ \forall \mathbf{x} \in \partial\Omega_u\} \tag{1a}$$

$$\delta\mathbf{u}(\mathbf{x}) \in \mathscr{V}_u := \{\delta\mathbf{u} | \delta\mathbf{u}(\mathbf{x}) = \mathbf{0}\ \forall \mathbf{x} \in \partial\Omega_u\} \tag{1b}$$

$$d(\mathbf{x}) \in \mathscr{U}_d := \{d | d(\mathbf{x}) \in [0,1], \dot{d} \geq 0\ \forall \mathbf{x} \in B; d(\mathbf{x}) = 1\ \forall \mathbf{x} \in S\} \tag{1c}$$

$$\delta d(\mathbf{x}) \in \mathscr{V}_d := \{\delta d | \delta d(\mathbf{x}) \geq 0\ \forall \mathbf{x} \in B; \delta d(\mathbf{x}) = 0\ \forall \mathbf{x} \in S\} \tag{1d}$$

The key concept of the phase field method is to regularize a sharp crack surface A_s over a localization band B using the diffused functional A_d, such that

$$A_d = \int_B \gamma(d, \nabla d)\, dV \approx A_s = \int_B \delta_s\, dV \tag{2}$$

in which γ is the crack density function which is approximating the Dirac delta function along a sharp crack. Following [25], the crack density function is defined as

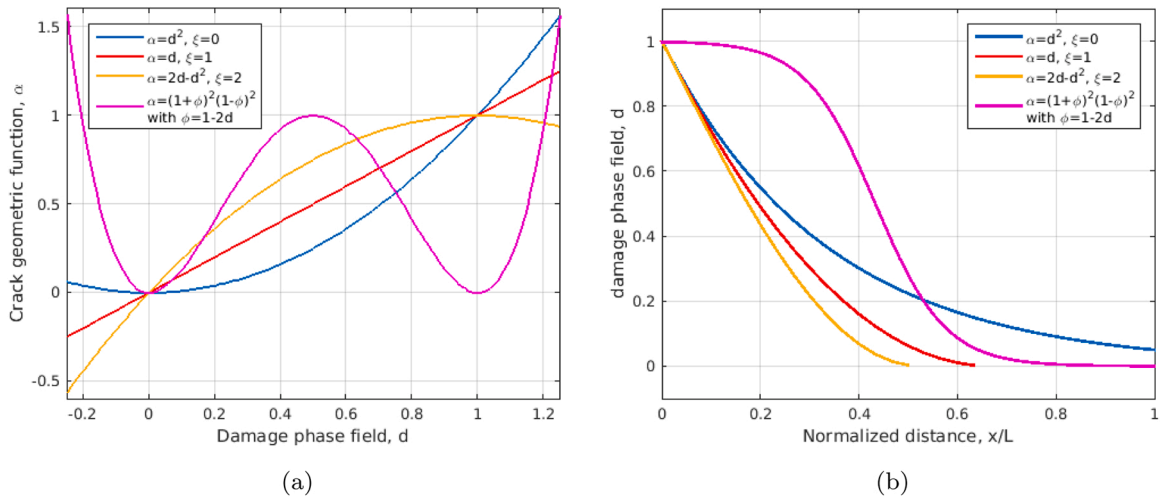

Fig. 2. Crack geometric functions (left); spatial distribution of damage phase field for different crack geometric functions (right).

$$\gamma(d,\nabla d)=\frac{1}{c_o}\left(\frac{1}{b}\alpha(d)+b\left|\nabla d\right|^2\right)\quad \text{with } c_o=4\int_0^1\sqrt{\alpha(\beta)}d\beta \tag{3}$$

in which b is the length scaling factor describing the width of the regularization band, c_o is a regularization functional such that the diffused area A_d represents the crack surface A_s and $\alpha(d)$ is the crack geometric function characterizing the distribution of the crack phase field. The crack geometric function $\alpha(d)$ is assumed to satisfy the following conditions: $\alpha(0)=0$, $\alpha(1)=1$.

2.1. Crack geometric function

Various forms of crack geometric functions are used in literature. They can be divided into two main categories (i) Double-well function and (ii) monotonic functions. [28] and [31] used a double-well crack geometric function ($\alpha=(1+\phi)^2(1-\phi)^2$ with $\phi=1-2d$) for the simulation of damage in asphalt mixtures, Fig. 2a. Such a function was developed in the physics community to model phase transformation problems, see for example [32]. The phase field model employing a double-well function for fracturing solids inherently assumes that there exist an energetic equivalence between the damaged ($d=1$) and undamaged ($d=0$) states. Consequently, there is an equal tendency of a crack to grow perpendicular to the actual crack path. This results in unrealistic crack widening and lateral crack growth [27,33–35]. Therefore, the double-well function is not well suited to model crack propagation problems. For this reason, monotonic crack geometric functions are more preferred for simulating fracture in solids, see for example [23,26,27,33].

[21] and [22] used a single-well crack geometric function defined as $\alpha=d^2$ in their phase field model for brittle fracture. The function is a natural choice because it automatically gives the minimizer of the total potential at $d=0$ in the absence of mechanical strains. Fig. 2b shows the distribution of damage phase field in a 1-D bar of length $\pm L$ for a crack centered at $x=0$. It is evident from the figure that the function $\alpha=d^2$ gives an infinite width of the localization band. [36] proposed a linear crack geometric function defined as $\alpha=d$. However, the boundedness of the damage phase field, i.e. $d\in[0,1]$, cannot be intrinsically guaranteed and special strategies have to be used to ensure phase field boundedness [37–39]. [25] proposed the following generic form of the crack geometric function

$$\alpha=\xi d+(1-\xi)d^2 \tag{4}$$

It is interesting to note that the crack geometric functions proposed by [21] and [36] can be recovered from equation (4) using $\xi=0$ and $\xi=1$, respectively, Fig. 2a. [25] advocated the use of a monotonic crack geometric function defined as $\alpha=2d-d^2$ with $\xi=2$. The value $\xi=2$ is the optimal value which also ensures damage irreversibility, i.e $\dot{d}\geq 0$ [25]. The function $\alpha=2d-d^2$ gives a finite localization bandwidth, Fig. 2b. The property of finiteness of the localization bandwidth is also important from the numerical modelling point of view. By virtue of finiteness of localization band, the phase field model can be applied to a small portion of a body, thereby reducing the computational cost. Note, that the localization band for the double-well function is also infinite, Fig. 2b. Moreover, for the functions $\alpha=d$ and $\alpha=2d-d^2$ boundedness condition ($0\leq d\leq 1$) has to be dealt carefully and special strategies have to be used to ensure boundedness of the phase field [37–39]. In this paper, the crack geometric function $\alpha=2d-d^2$ is used.

2.2. Governing equations

The total potential energy Π of a solid body comprises of the internal strain energy Π^{int}, fracture energy Π^{f} and external potential energy Π^{ext} given as [25,30].

$$\Pi(\mathbf{u},d)=\underbrace{\int_{\Omega}\omega(d)\Psi_o\,dV}_{\Pi^{int}}+\underbrace{\int_{\Omega}G_f\gamma(d,\nabla d)\,dV}_{\Pi^{f}}-\underbrace{\int_{\Omega}\overline{\mathbf{b}}\cdot\mathbf{u}\,dV-\int_{\partial\Omega_t}\overline{\mathbf{t}}\cdot\mathbf{u}dA}_{\Pi^{ext}} \tag{5}$$

in which G_f is the fracture energy, ω is the degradation function which takes into account the degradation of the elastic strain energy Ψ_o due to damage. The degradation function is defined as [25].

$$\omega(d)=\frac{(1-d)^p}{(1-d)^p+a_1 d\cdot P(d)}\quad P(d)=1+a_2 d+a_3 d^2 \tag{6}$$

The advantage of using the above form of degradation function compared to the models presented in [21,22,26,28] is, that any type of softening behavior can be modelled. This feature is important as it enables the phase field model to simulate a quasi-brittle behavior of fracturing solids. The parameters p, a_1, a_2 and a_3 are determined to recover most commonly used cohesive constitutive laws. a_1 is the only parameter which is dependent on length scale factor b and material properties. It is defined as

$$a_1=\frac{2\xi l_{cz}}{c_o b}\quad \text{for Irwin's characteristic length } l_{cz}=\frac{E_o G_f}{f_t^2} \tag{7}$$

2.3. Weak and discretized form of equilibrium

Weak form of the governing equations are obtained by the minimization of the total potential, equation (5). The following coupled system of equations are obtained

$$-\int_{\Omega}\left(\frac{\partial\Psi}{\partial\epsilon}:\nabla^{sym}\delta\mathbf{u}\right)\mathrm{dV}+\int_{\Omega}\overline{\mathbf{b}}\cdot\delta\mathbf{u}\,\mathrm{dV}+\int_{\Omega_t}\overline{\mathbf{t}}\cdot\delta\mathbf{u}\,\mathrm{dA}=\mathbf{0} \tag{8}$$

$$\int_{B}(\omega'\overline{Y}\delta d)\mathrm{dV}+\int_{B}\frac{G_f}{c_o}\left(\frac{1}{b}\alpha'\delta d+2b\,\nabla d\cdot\nabla\delta d\right)\mathrm{dV}\le 0 \tag{9}$$

It is assumed that the bulk material response of asphalt mixtures can be modelled using elastic constitutive law at low temperatures. Therefore, temperature and rate effects are not included in this paper. All numerical tests are performed at a single low temperature. In this work, a linear relationship between a Cauchy stress ($\boldsymbol{\sigma}$) and small strain tensor ($\boldsymbol{\epsilon}$) is used

$$\boldsymbol{\sigma}=\frac{\partial\Psi}{\partial\boldsymbol{\epsilon}}=\omega\frac{\partial\Psi_o}{\partial\boldsymbol{\epsilon}}=\omega(\mathbf{D}:\boldsymbol{\epsilon})=\omega(\mathbf{D}:\nabla^{sym}\delta\mathbf{u})=\omega\,\boldsymbol{\sigma}_o \tag{10}$$

in which $\boldsymbol{\sigma}_o$ is the effective stress tensor, $\mathbf{D}$ is the material elastic stiffness tensor and $\nabla^{sym}\mathbf{u}$ denotes the symmetric part of displacement gradient. $\overline{Y}$ denotes the effective damage driving force. It is considered in this work that damage initiates when the local tensile principle stress reaches the tensile strength of a material. A history variable H is introduced to ensure damage irreversibility [22].

$$H=\max_{t\le T}\left(\frac{f_t^2}{2E_o},\overline{Y}_t\right),\qquad \overline{Y}_t=\left(\frac{1}{2E_o}(\sigma_1)^2\right) \tag{11}$$

Accordingly, the effective damage driving force $\overline{Y}$ is replaced with H in equation (9). This sufficiently guarantees the irreversibility condition $\dot{d}(\boldsymbol{x})\ge 0$ and a non-negative damage phase field $d(\boldsymbol{x})<0$.

Remark 2. In the author's experience, the boundedness of the phase field is seldom violated using the history variable. Therefore, no other special strategies have been used in the numerical implementation for damage boundedness.

Within the framework of finite elements, the domain Ω is discretized into n_e number of finite elements. The approximated displacement and damage phase field are given as

$$\mathbf{u}(\mathbf{x})=\mathbf{N}_i^u(\mathbf{x})\,\mathbf{a}_i^u,\quad \delta\mathbf{u}(\mathbf{x})=\mathbf{N}_i^u(\mathbf{x})\,\delta\mathbf{a}_i^u \tag{12}$$

$$d(\mathbf{x})=N_i^d(\mathbf{x})\,a_i^d,\quad \delta d(\mathbf{x})=N_i^d(\mathbf{x})\,\delta a_i^d, \tag{13}$$

with

$$\mathbf{N}_i^u=N_i\mathbf{I},\quad N_i^d=N_i \tag{14}$$

in which $\mathbf{a}_i^u$ and a_i^d are the unknown nodal displacement and damage phase field degrees of freedom (dofs) for node i, respectively. $\mathbf{I}$ is the identity tensor and N_i is the standard finite element shape function for node i. Accordingly, the strain field and the gradient of damage phase field are given as

$$\boldsymbol{\epsilon}(\mathbf{x})=\nabla^{sym}\mathbf{u}(\mathbf{x})=\mathbf{B}_i^u(\mathbf{x})\mathbf{a}_i^u,\qquad \delta\boldsymbol{\epsilon}(\mathbf{x})=\nabla^{sym}\delta\mathbf{u}(\mathbf{x})=\mathbf{B}_i^u(\mathbf{x})\delta\mathbf{a}_i^u \tag{15}$$

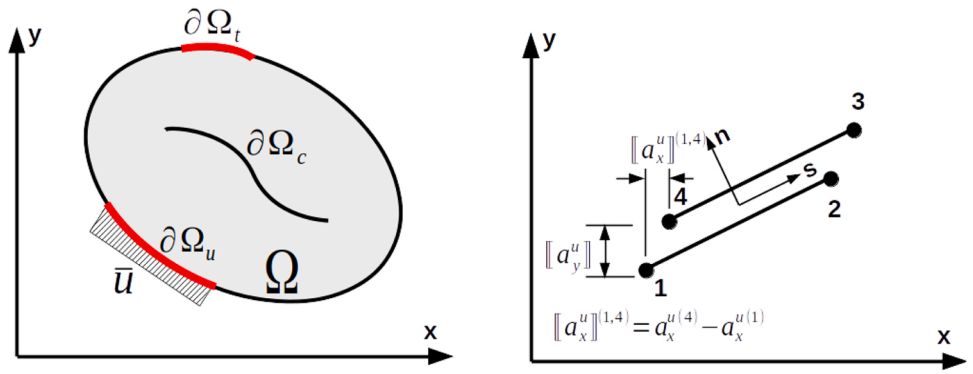

(a) A solid body with a crack (b) 4-noded interface element

Fig. 3. Solid body with a crack (left); 4-noded interface element (right) [[**a**]] shows the relative displacement for the pair of nodes 1 and 4.

$$\nabla d(\mathbf{x}) = \mathbf{B}_i^d a_i^d, \qquad \nabla\,\delta d(\mathbf{x}) = \mathbf{B}_i^d \delta a_i^d \tag{16}$$

in which the matrices $\mathbf{B}_i^u$ and $\mathbf{B}_i^d$ for a 2D finite element analysis are given as

$$\mathbf{B}_i^u = \begin{bmatrix} \partial_x N_i & 0 \\ 0 & \partial_y N_i \\ \partial_y N_i & \partial_x N_i \end{bmatrix}, \qquad \mathbf{B}_i^d = \begin{bmatrix} \partial_x N_i \\ \partial_y N_i \end{bmatrix} \tag{17}$$

Incorporating the approximations, i.e. equations (12), (13), (15) and (16) into the weak form, i.e. equations (8) and (9), the following two discretized equations are obtained

$$\mathbf{R}^u = \int_\Omega (\mathbf{N}^u)^T \bar{\mathbf{b}}\, \mathrm{dV} + \int_{\partial\Omega_t} (\mathbf{N}^u)^T \bar{\mathbf{t}}\, \mathrm{dA} - \int_\Omega (\mathbf{B}^u)^T \boldsymbol{\sigma}\, \mathrm{dV} = \mathbf{0} \tag{18}$$

$$\mathbf{R}^d = -\int_\Omega (\mathbf{N}^d)^T \left(\omega' H + \frac{G_f}{c_o b}\alpha'\right) \mathrm{dV} - \int_\Omega (\mathbf{B}^d)^T \left(\frac{2b}{c_o} G_f \nabla d\right) \mathrm{dV} \le \mathbf{0} \tag{19}$$

More details of the model can be found in [30].

3. Interface element formulation

This section briefly discusses the governing equations of the interface element for the sake of completeness. Consider a solid body with domain Ω subjected to external tractions $\bar{\mathbf{t}}$ and body forces $\bar{\mathbf{b}}$. The body also contains an internal crack surface $\partial\Omega_c$, Fig. 3.

Within the framework of finite element method, the body is discretized with n_E number of finite elements. Interface elements are inserted along finite element boundaries to simulate a crack. The displacement vector ($\mathbf{a}_c^u$) is arranged as

$$\mathbf{a}_c^u = \begin{bmatrix} \mathbf{a}_{c,top}^u & \mathbf{a}_{c,bottom}^u \end{bmatrix}^T \tag{20}$$

$\mathbf{a}_c^u$ is the displacement degrees of freedom of set of nodes along the crack. The relative displacement/displacement jump at the crack interface is defined as

$$[\mathbf{u}] = \mathbf{N} * \begin{bmatrix} \mathbf{a}_{c,top}^u \\ \mathbf{a}_{c,bottom}^u \end{bmatrix} \qquad \text{with } \mathbf{N}* = [\bar{\mathbf{N}} \quad -\bar{\mathbf{N}}] \tag{21}$$

For a four-noded cohesive element $\bar{\mathbf{N}} = [N_1\mathbf{I} \quad N_2\mathbf{I}]$. The discretized equilibrium equation is given as

$$\begin{aligned} \mathbf{R}^u \;=\; & \int_\Omega (\mathbf{N}^u)^T \bar{\mathbf{b}}\, \mathrm{dV} + \int_{\partial\Omega_t} (\mathbf{N}^u)^T \bar{\mathbf{t}}\, \mathrm{dA} - \int_\Omega (\mathbf{B}^u)^T \boldsymbol{\sigma}_o\, \mathrm{dV} \\ & + \int_{\partial\Omega_c} (\mathbf{N}*)^T \mathbf{t}_c\, \mathrm{dA} = \mathbf{0} \end{aligned} \tag{22}$$

in which $\mathbf{N}^u$ is the matrix of shape functions as defined in equation (14) and $\mathbf{N}$ * is the matrix of shape function to approximate the relative displacement at the interface. Note that there is no effect of interface damage on the bulk material and therefore $\boldsymbol{\sigma}_o$ is used instead of $\boldsymbol{\sigma}$ in equation (22). The two sides of the cracked body are interacting through the tractions at the interface $\partial\Omega_c$. Whereas in

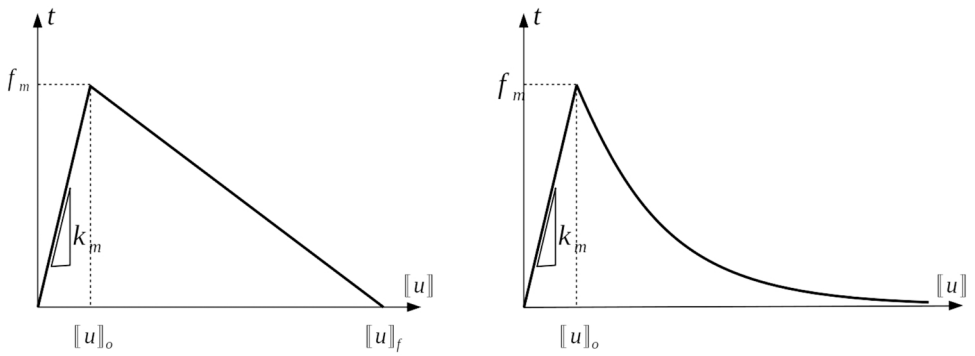

(a) Bi-linear cohesive law (b) Exponential cohesive law

Fig. 4. Cohesive constitutive laws used in interface element analysis.

case of phase field damage model an area around the crack experiences damage. Moreover, in the interface element formulation, separate constitutive laws are used for bulk material and cohesive interface. Whereas a unified constitutive law is used for the whole material in phase field models.

Two types of cohesive constitutive laws, namely the bilinear and exponential cohesive laws, Fig. 4 are used in this work. A brief detail of each of the constitutive law is given below

- *Bi-linear cohesive constitutive law:* The traction vector, $\mathbf{t}_c$ in the local crack coordinate system is defined as

$$\mathbf{t}_c = [\mathbf{I} - d\,\mathbf{P}]k_m[\mathbf{u}] \quad \text{with } d = \max_{\tau \le t} \begin{cases} 0 & [u] \le [u]_o \\ \dfrac{[u]_f([u] - [u]_o)}{[u]([u]_f - [u]_o)} & [u]_o < [u] < [u]_f \\ 1 & [u] \ge [u]_f \end{cases} \tag{23}$$

in which $\mathbf{I}$ is a 2×2 identity matrix and $\mathbf{P}$ is defined as

$$\mathbf{P} = \begin{bmatrix} \dfrac{\langle [u]_n \rangle}{[u]_n} & 0 \\ 0 & 1 \end{bmatrix} \quad \text{with } \langle [u]_n \rangle = ([u]_n + |[u]_n|)/2 \tag{24}$$

$[[u]]$ is the equivalent displacement jump, $[[u]]_o$ is equivalent displacement jump corresponding to peak failure strength f_m and $[[u]]_f$ is the equivalent displacement jump at full decohesion. Details of the bi-linear cohesive model can be found in [40].

- *Exponentially decaying softening law:* The traction vector in the local crack coordinate system is defined as

$$\mathbf{t}_c = [\mathbf{I} - d\,\mathbf{P}]k_m[\mathbf{u}] \quad \text{with } d = \max_{\tau \le t} \begin{cases} 0 & [u] \le [u]_o \\ 1 - exp\left(\dfrac{-f_m}{G_f}\left([u] - [u]_o\right)\right)\left(\dfrac{[u]_o}{[u]}\right) & [u] > [u]_o \end{cases} \tag{25}$$

f_m and G_f are the mixed mode material strength and fracture toughness, respectively. The quantities $[[u]]$, $[[u]]_o$, f_m and G_f are defined similar to [40]. These laws are identical to the softening laws used in phase field model, PFM-model2, in section 4.

4. Numerical results and discussions

In this section several numerical examples are presented to compare the performance of different phase field models. The phase field and interface element models are implemented in an in-house finite element code written in a C+ + object oriented environment. The pseudo codes of the phase field and interface element models are given in the Appendix A, algorithmic boxes 1 and 2, respectively.

Two variants of phase field model are used in the analyses, i.e phase field model of [23] later referred to as PFM-model1 and phase field model of [25] later referred to as PFM-model2. PFM-model2 is simulated with different softening laws. The PFM-model2 parameters (c_o, p, a_1, a_2, a_3) can be determined based on the given material properties and the desired softening law [25]. The phase field model parameters used in the analyses are given in Table 1. Note that the a_1 is the only parameter which depends upon given material properties and is calculated using equation (7).

All numerical analyses are performed using two dimensional four node quadrilateral elements. In case of phase field analysis, the phase field degree of freedom ($a_i^d = d$) is also added at each node i in addition to the displacement degrees of freedom ($\mathbf{a}_i^u = [u_x, u_y]^T$).

In the subsequent sections, first an analysis of a single edge notch specimen is presented. The specimen is analyzed with the PFM-

Table 1
Phase field model parameters.

Model	c_o	ξ	p	a_1	a_2	a_3
PFM-model1	2	0	2	2	− 0.5	0
PFM-model2 with linear softening behavior	π	2	2	$\frac{4l_{cz}}{\pi b}$	− 0.5	0
PFM-model2 with exponential softening behavior	π	2	2.5	$\frac{4l_{cz}}{\pi b}$	0.1748	0
PFM-model2 with softening curve of Cornellisson	π	2	2	$\frac{4l_{cz}}{\pi b}$	1.3868	0.6567

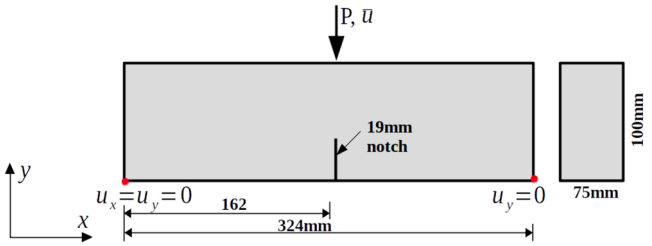

Fig. 5. Geometry and boundary conditions of single edge notch specimen.

Table 2
Calibrated material properties from different researchers.

	Experimental [3]	Calibrated [30]	Calibrated [6]	Calibrated [3]
Tensile strength f_t(MPa)	3.56	3.40	3.21	3.92
Fracture toughness G_f(N/mm)	0.344	0.344	0.241	0.241

model1 and PFM-model2 to investigate the suitability and appropriateness of the phase field model for damage modeling in asphalt mixtures. Numerical results are also compared with the interface element analysis for completeness. Additionally, the effect of softening laws on structural response and damage progression is investigated. The second example presents a parametric study to look into the influence of different phase field model parameters on the response.

4.1. Single edge notch (SEN) specimen - three point bending test

A single edge notch beam test is simulated to investigate the performance of three damage models, i.e PFM-model1, PFM-model2 and cohesive zone model with interface elements. Geometry and boundary conditions of the single edge notch beam is shown in Fig. 5. A finite element mesh of quadrilateral elements is used for the three analyses. Analysis with PFM-model1 and PFM-model2 are performed with the same finite element mesh. A fine mesh with a maximum element size of 1 mm is used near the prospective crack growth region and a mesh size of 5 mm is used elsewhere. In order to perform finite element analysis with cohesive zone model, interface elements of size 1 mm are inserted along the full depth of the beam ahead of the notch tip. A bi-linear cohesive constitutive law is used to simulate the interfacial behavior. A dummy interface stiffness of $k_m = 1e8$ N/mm is used in the analyses, which is high enough to simulate an initially rigid interface yet low enough to avoid numerical instabilities. A displacement control analysis is performed with an increment of 0.001 mm.

The material considered for the analyses is an asphalt mixture consisted of asphalt binder PG (Performance Grade) 64–22 and nominal maximum aggregate size of 9.5 mm [3]. The material has been experimentally investigated by [41] and [3]. The authors [3, 41] used indirect tension test at − 10°C to determine tensile strength of the mixture. Whereas, a single edge notch beam test at − 10°C was performed to obtain mode-I fracture toughness (G_f) of the material. The Young's modulus (E_o) was obtained from a complex modulus testing of the mixture at 10°C and 1 Hz. Due to the low test temperature, it is assumed that the numerical analysis can be performed using elastic material properties. Several researchers have analyzed the same single edge notch beam using different numerical models. For example, [3] used interface elements, [6] used discrete element modelling approach whereas [30] used phase field model to simulate model-I fracture in the beam. The calibrated fracture parameters (f_t and G_f) used in different models are given in Table 2. Material properties used for the numerical investigation in this paper are given in Table 3. Note, that in this paper the phase field analyses are conducted with the calibrated values of [30], whereas interface element analysis is performed with the calibrated values of [3]. Analysis is performed by considering homogenized material properties of asphalt mixtures. A more detailed analysis can be performed by considering the micro-structure details of asphalt mixtures, however, this is out of scope of this manuscript. Firstly, because the aim here is to discuss numerical aspects of the phase field model and secondly, it was shown in [30] that the phase field

Table 3
Material properties used in the analyses.

	PFM-model1	PFM-model2	interface elements
Young's modulus, E_o(GPa)	14.2	14.2	14.2
Poisson ratio, ν	0.35	0.35	0.35
tensile strength, f_t(MPa)	–	3.4	3.92
fracture toughness, G_f(N/mm)	variable	0.344	0.241

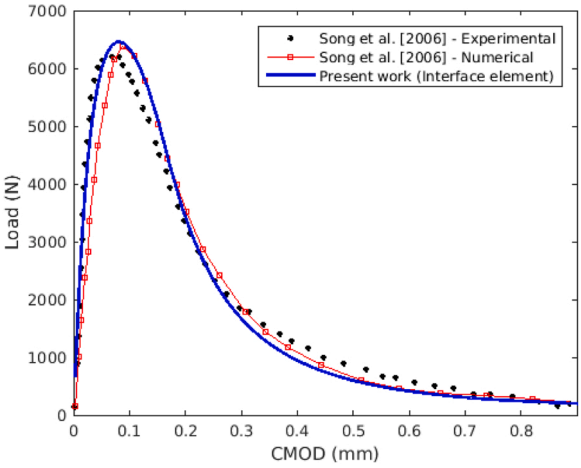

Fig. 6. Load versus CMOD curve using interface element analysis.

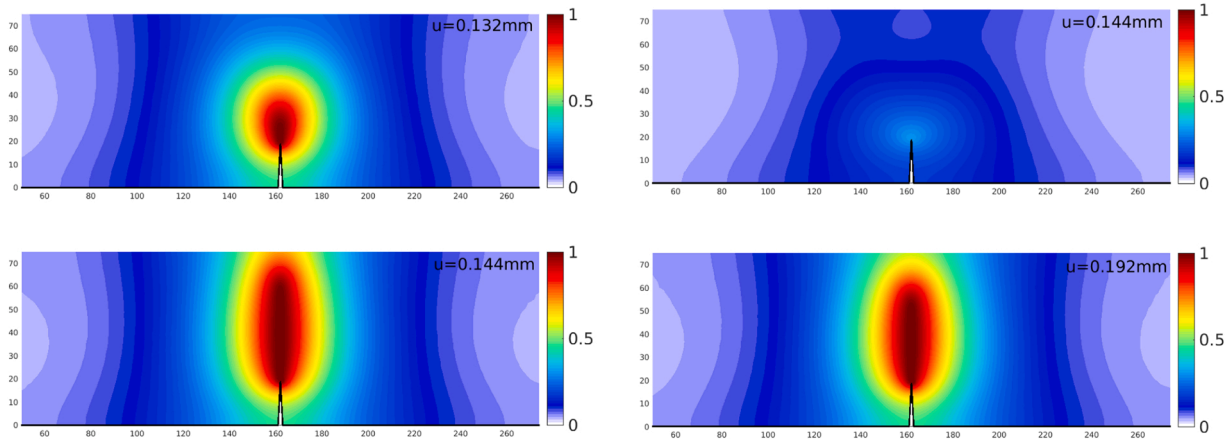

Fig. 7. Damage profiles using PFM-model1 with b= 20 mm at different prescribed displacements, left: $G_f = 0.12$ N/mm, right: $G_f = 0.241$ N/mm.

model with cohesive zone model is sufficient to capture the global response and general damage pattern in asphalt mixtures.

4.1.1. Analysis results of SEN with interface elements

Figure 6 shows the load versus crack mouth opening displacement (CMOD) curve in comparison with the experimental result [3]. The result of the analysis is in good agreement with the experimental results. It is observed that the interface element analysis is able to capture the initial portion of the curve, the peak load and the post peak behavior of asphalt mixture. Fig. 6 also presents the numerical results of [3]. [3] used a potential based exponential cohesive constitutive law [4] to simulate model-I cracking in SEN beam.The numerical results of [3] does not correctly simulates the initial stiffness branch of the curve. This is due to the initial compliance of the adopted cohesive constitutive law. The problem can be solved using an interface law with an initial high stiffness as used in the present contribution.

4.1.2. Analysis result of SEN with PFM-model1

The analysis using PFM-model1 is performed for a range of model parameters $b = 20$, 50, 100 mm and $G_f = 0.12$, 0.241 N/mm.

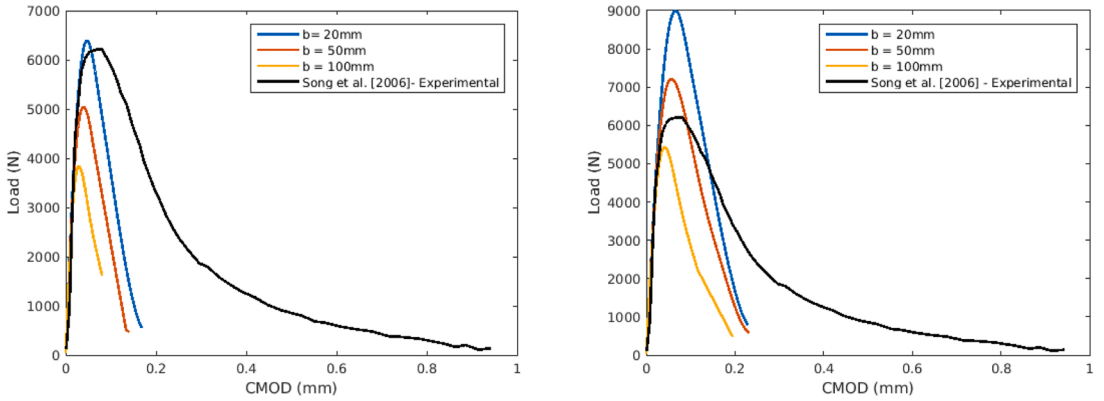

(a) Effect of length scaling factor, b with G_f = 0.12N/mm (b) Effect of length scaling factor, b with G_f = 0.241N/mm

Fig. 8. Load Vs CMOD curves of SEN beam with PFM-model1 (a) Effect of length scaling factor, b with $G_f = 0.12$ N/mm; (b) Effect of length scaling factor, b with $G_f = 0.241$ N/mm.

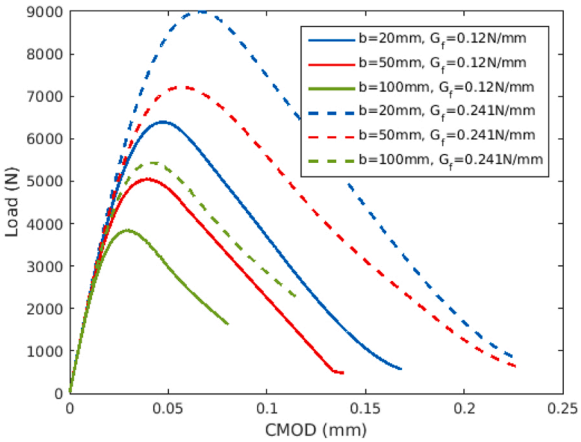

Fig. 9. Effect of length scaling factor and fracture toughness on response of SEN using PFM-model1.

Fig. 7 shows damage profiles obtained with an analysis using $b = 20$ mm and $G_f = 0.12$, 0.241 N/mm at different displacement increments. It is observed that the damage profiles are qualitatively correctly simulated and represents mode-I fracture in the beam. Furthermore, the damage spreads over the whole beam even though it is negligibly small in regions far from the notch. This is due to the type of crack geometric function ($\alpha = d^2$) used in PFM-model1 which gives an infinite localization bandwidth.

Figure 8a and b compares the PFM-model1 analysis results with the experimental load versus CMOD curve for different values of length scaling factor b and fracture toughness G_f. It can be observed from the figures that the initial branch of the curve (before the peak load) and the peak load for typical values of b matches the experimental result, but the post peak branch (softening branch) does not match the experimental result. Moreover, peak load increases with the decreasing value of length scaling factor b. Furthermore, changing the model parameters b and G_f do not help to calibrate the PFM-model1 with the experimental result. Therefore, it is concluded that only predicting the qualitative damage profiles and peak loads (for some values of b) are not enough to correctly represents the material response. Moreover, increasing the values of parameter b for a particular fracture toughness G_f, not only increases the peak load but also increases the width of the curve. However, slope of the softening branch almost remains unchanged. It is also evident from the figures that the softening branch drops quickly comparative to the experimental result for all values of b and G_f. It is observed from the figure that the parameters b and G_f are only scaling the load versus CMOD curves whereas shape of the curve does not change, Fig. 9. This indicates that PFM-model1 is essentially simulating brittle material behavior and therefore not suitable for simulating quasi-brittle behavior of asphalt concrete even at low temperatures where its response is nearly brittle. Moreover, the length scaling factor b appears to be a material parameter which is a function of the peak load.

4.1.3. Analysis result of SEN with PFM-model2

Figure 10 presents the PFM-model2 analysis results for different values of f_t and G_f. The analysis is performed with $b = 5$ mm. It has

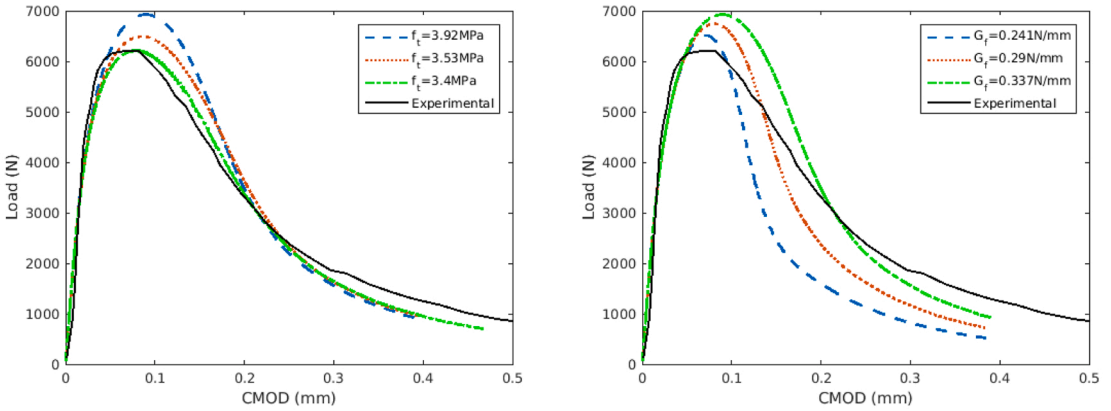

(a) Effect of tensile strength, f_t with $G_f = 0.337N/mm$ (b) Effect of fracture toughness, G_f with $f_t = 3.92MPa$

Fig. 10. Load versus CMOD curves of SEN using PFM-model2 (a) Effect of tensile strength, f_t with $G_f = 0.337N/mm$; (b) Effect of fracture toughness, G_f with $f_t = 3.92MPa$.

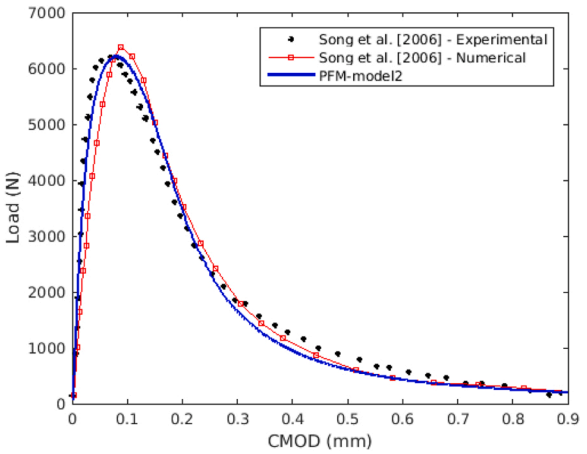

Fig. 11. Load versus CMOD curve of SEN using PFM-model2.

been shown in [30] that PFM-model2 results are not sensitive to b unless it is chosen as small as to resolve the damage phase field. This is further demonstrated in subsequent sections. Fig. 10a presents the effect of tensile strength on the response. It can be observed that increase in f_t affects the peak load whereas remaining part of the curve remains unaffected as opposed to PFM-model1. Fig. 10 shows the effect of fracture toughness G_f on the response. It is observed that increasing the value of G_f increases the width of the curve, thereby increasing the area under the curve with a slight increase in peak load. Therefore, two parameters (f_t and G_f) can be easily adjusted to calibrate the model with experimental data compared to PFM-model1. Fig. 11 shows the analysis results using the calibrated values of f_t and G_f. The result is in good agreement with the experimental data. The PFM-model2 is able to capture the pre-peak response, peak load and post-peak response of the single edge notch beam test. Thus, it can be concluded that PFM-model2 is more suitable to simulate the behavior of asphalt concrete compared to PFM-model1. It is interesting to note here that the calibrated material properties (f_t = 3.4 MPa, G_f = 0.344 N/mm) are close to the experimentally determined values (f_t = 3.56 MPa, G_f = 0.344 N/mm) in [3].

4.1.4. Comparison between PFM-model2 and interface element analysis

For comparison, the PFM-model2 analysis is performed with the fracture properties similar to the interface element analysis, i.e. f_t = 3.92 MPa and G_f = 0.241 N/mm and using a linear softening behavior. The material properties used for the analysis of interface element analysis are given in Table 3. Fig. 12a compares the load versus CMOD curves for the two analyses and Fig. 12b compares the dissipated energy. It is evident from the figures that PFM-model2 analysis gives smaller peak load, smaller area under the curve compared to the interface element analysis for the same values of tensile strength f_t and fracture toughness G_f. Additionally, more energy is dissipated in case of phase field analysis compared to the interface element analysis. This is because that in case of interface

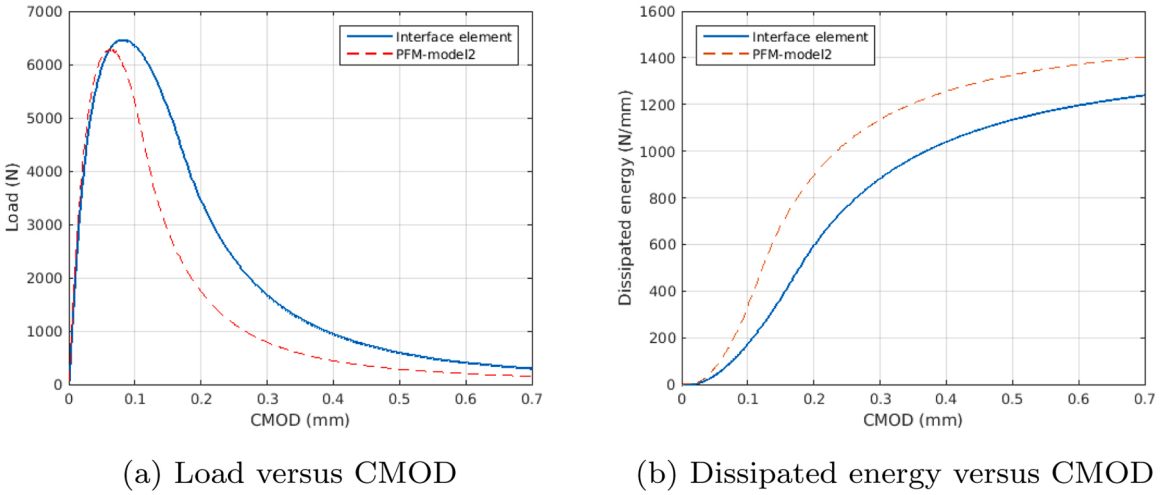

Fig. 12. Comparison of PFM-model2 and interface element results (a) Load versus CMOD; (b) Dissipated energy versus CMOD.

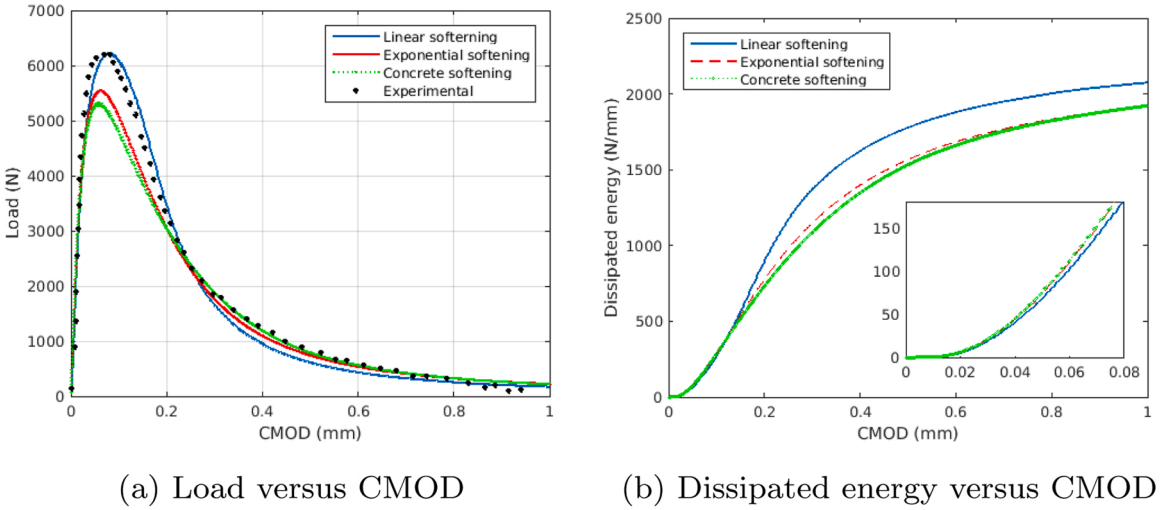

Fig. 13. Comparison of SEN response with different softening laws (a) Load versus CMOD; (b) Dissipated energy versus CMOD.

element analysis all material non-linearities are concentrated over an interface of zero-thickness therefore the energy is only dissipated along the main crack. Whereas, in phase field analysis the damage is smeared over a volume therefore the energy is dissipated not only along the main crack but also in regions around the main crack. Hence, the model parameters f_t and G_f, even though they have similar meaning in the two analyses models, they are required to be calibrated separately for the two damage models. Furthermore, the calibrated material properties for the case of phase field model are more closely related to the experimentally determined values. Moreover, the interface element analysis uses different constitutive laws for the interface and bulk material, therefore the model is anisotropic. On the other hand, phase field model uses the same constitutive law for the whole bulk material. Therefore, it can be concluded that there is no one to one relationship between the fracture material properties of phase field and interface element models.

4.1.5. Effect of softening behavior

To investigate the effect of softening law on the material response the PFM-model2 analysis using three softening laws namely linear, exponential and Cornelissen softening law [42] is performed. The model parameters to simulate a particular softening behavior are given in Table 1.

Figure 13a compares the response with three different softening laws in terms of load versus CMOD curves. It is observed that the linear softening model gives a large peak load compared to the other two models, however, the post peak response is almost similar. Similar observations were also made by [43]. The load drop in case of exponential and Cornelissen softening models is due to rapid softening of the material after the peak stress. Fig. 13b compares the dissipated energy for the three softening models. It is observed that more energy is dissipated in case of linear softening model. Moreover, in case of linear softening law the rate of energy dissipation

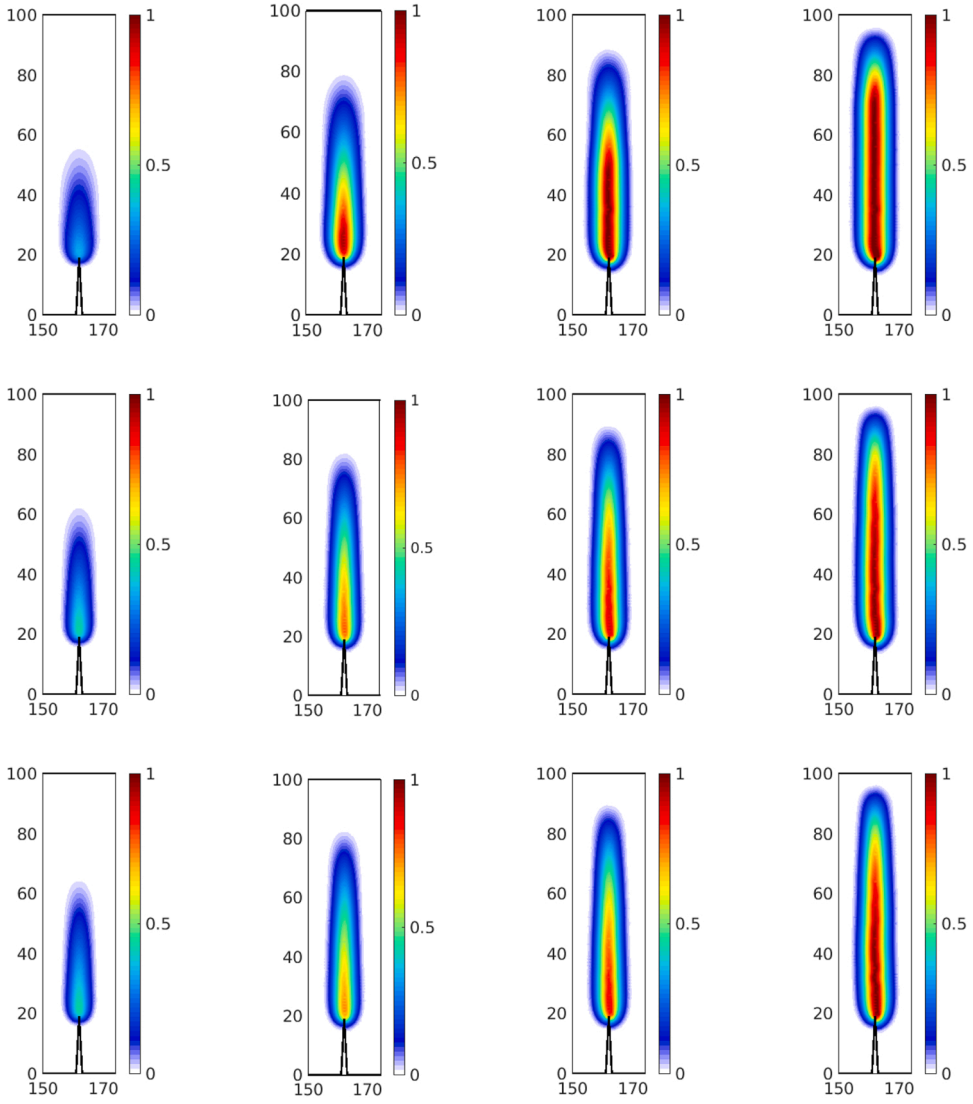

Fig. 14. Comparison of SEN response with different softening behaviors. Damage profiles for linear, exponential and Cornelissen softening law (top to bottom) at prescribed displacement u = 0.14 mm, 0.21 mm, 0.28 mm, 0.49 mm (left to right).

is slow at the beginning but later the rate of energy dissipation increases compared to the exponential and Cornelissen softening model. Thereby, resulting in more energy dissipation. After CMOD = 0.3 mm there is no relative increase in dissipated energy among different models.

The effect of load reduction is also noticeable from Fig. 14. Fig. 14 shows a zoomed-in view of the damage profiles at various levels of prescribed displacements: u = 0.14 mm, 0.21 mm, 0.28 mm and 0.49 mm (left to right) for the softening models linear, exponential and Cornelissen (top to bottom), respectively. It is observed that at u = 0.14 mm, the damaged zone for the case exponential and concrete softening law is more elongated and shows more damage in the center region compared to linear softening. This early increased damage results in a lower peak load and more dissipated energy at the beginning in the case of exponential softening compared to the analysis with linear softening law for the same material parameters. This is not surprising because in the case of exponential softening the stress degrades exponentially and quickly after the initiation of damage whereas later on the stress decays slowly causing slow dissipation of energy. This causes reduced peak load and more elongated damaged zone for the case of exponential and Cornelissen softening models at the beginning and more damage for the case of linear softening model later on.

Fig. 15 compares the fully damaged region ($d > 0.95$) at u = 0.49 mm for the three softening models. It is evident that the length and width of fully damaged zone is more for the case of analysis with linear softening. This behavior is also due to the intrinsic nature of the softening curves. Exponential softening results in fast material degradation and therefore material does not have sufficient time for stress redistribution. On the contrary, linear softening results in relatively slow material degradation. Consequently, stress redistribution occurs and more area surrounding the crack is stressed. This increases the width of damage zone. Moreover, stress decays slowly

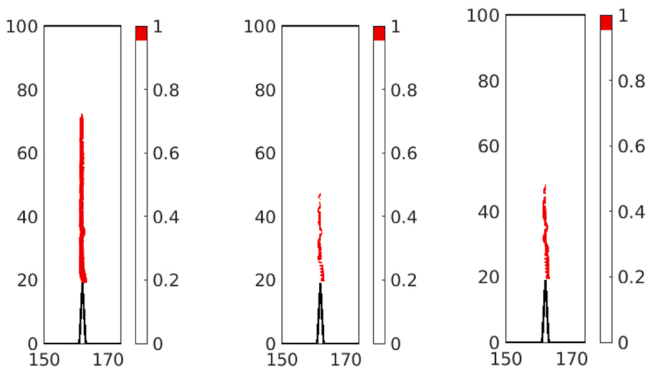

Fig. 15. Comparison of SEN response with different softening behaviors. Fully damaged zones for linear, exponential and Cornelissen softening law (left to right) at prescribed displacement u = 0.49 mm.

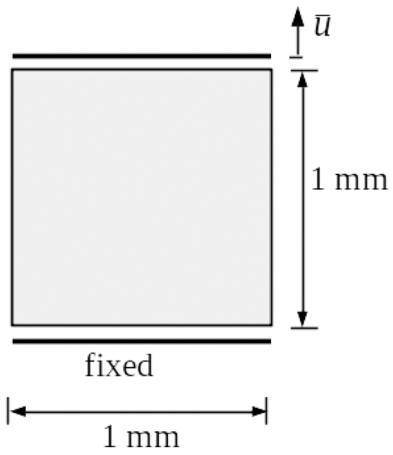

Fig. 16. Geometry and boundary conditions for the uniaxial test.

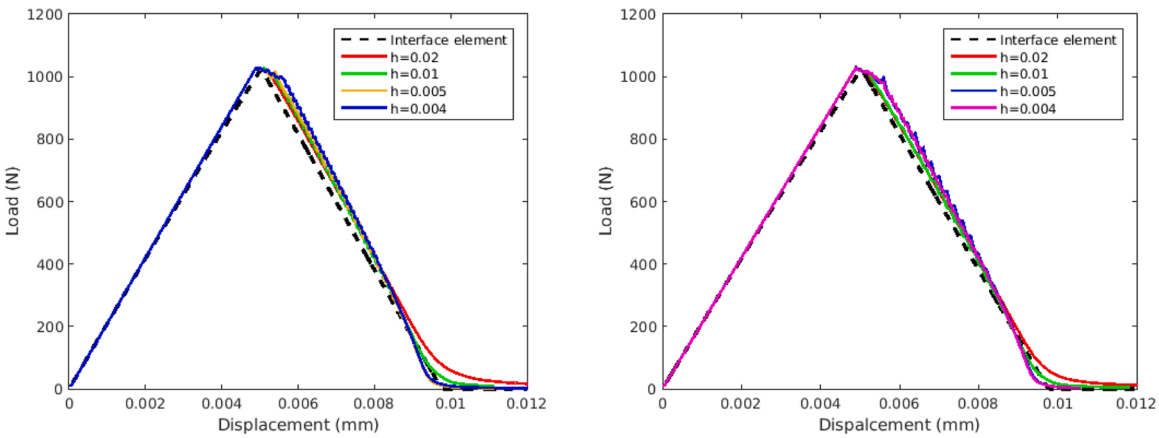

Fig. 17. Mesh size effect in a uniaxial tension test (a) b = 0.08 mm and b/h = 4, 8, 16, 20 (b) b = 0.1 mm and b/h = 5, 10, 20, 25.

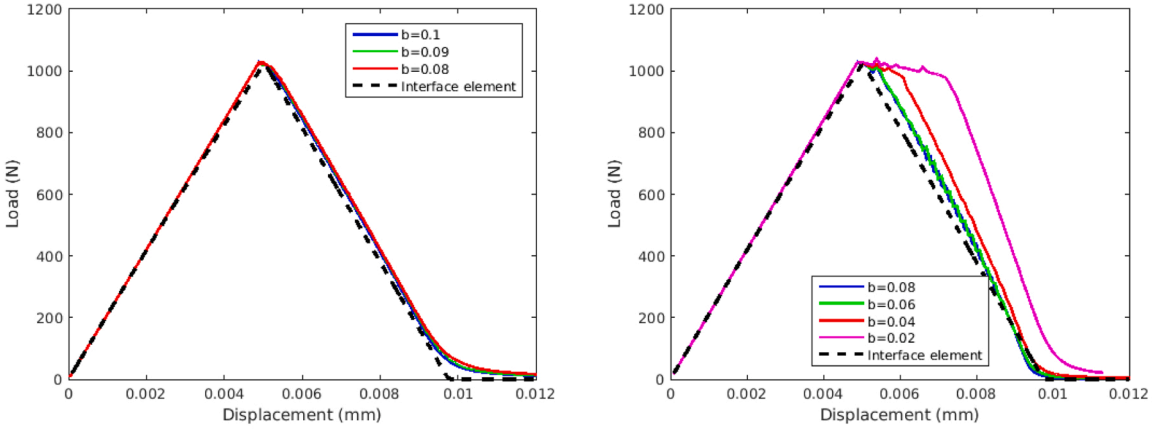

(a) h=0.02mm and b/h = 5, 4.5, 4 (b) h=0.004mm and b/h = 20, 15, 10, 5

Fig. 18. Effect of length scaling factor in a uniaxial tension test (a) h = 0.02 mm and b/h = 5, 4.5, 4; (b) h = 0.004 mm and b/h = 20, 15, 10, 5.

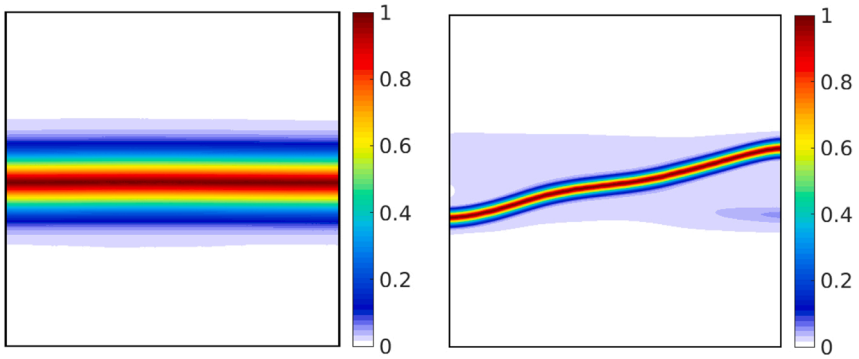

(a) Damage profile for b=0.08mm (b) Damage profile for b=0.02mm

Fig. 19. Damage profiles for mesh mesh size h = 0.004 mm and b = 0.08 mm(left), b = 0.02 mm(right) (a) Damage profile for b = 0.08 mm; (b) Damage profile for b = 0.02 mm.

later on in the exponential softening model causing a slow crack growth and less elongated fully damaged zone.

4.2. *Uniaxially loaded square plate*

To get a deep understanding of the effect of phase field model (PFM-model2) parameters, a simple geometry, i.e. a uniformly loaded plate in tension is analyzed. The geometry of the specimen is shown in Fig. 16. Since the aim here is to investigate effect of phase field model parameters irrespective of the type of material therefore a different set of material properties is used. The material properties used for the analysis are [44]: modulus of elasticity $E = 210$ GPa, $f_t = 1025$ MPa and $G_f = 5$ N/mm. The Poisson's ratio is taken as zero to simulate uniaxial stress state with no lateral strains. To prevent damage initiating near the point of application of load and near the supports, the material model is assumed to be elastic in these regions. For comparison, the analysis is also performed with the interface elements, in which case interface elements are inserted along the full width of the specimen at its mid height. Interface element analysis is performed with a dummy stiffness $k_m = 1e7$ N/mm.

4.2.1. *Effect of mesh size*

To investigate the effect of mesh size on the solution, the analysis is performed with different mesh sizes, h = 0.02, 0.01, 0.005 and 0.004 (h represents minimum element size in mm). Fig. 17 shows the analysis results for length scaling parameters, b = 0.1 and 0.08. It is evident from the figure that phase field model gives more stiff behavior until peak load whereas interface element analysis show some reduction in initial stiffness before attainment of peak load. Secondly, the post peak response for all meshes is similar to one another until full decohesion takes place. Near the point of full decohesion the phase field analysis result approaches the reference/interface element solution with mesh refinement. On the other hand, for the case of coarse mesh, the analysis result gradually approaches to a zero load and does not show a sharp change in load from loaded to unloaded state at the time of full decohesion. This is

Table 4
Comparison of peak load and percentage difference w.r.t interface element results.

		h = 0.02		h = 0.004	
	b/h (mm)	Peak load (N)	% difference	Peak load (N)	% difference
Interface element	–	1018.9	–	1018.9	–
PFM-model2	4	1029	0.99	–	–
PFM-model2	4.5	1030	1.09	–	–
PFM-model2	5	1030	1.09	1029	0.99
PFM-model2	10	–	–	1029	0.99
PFM-model2	15	–	–	1029	0.99
PFM-model2	20	–	–	1029	0.99

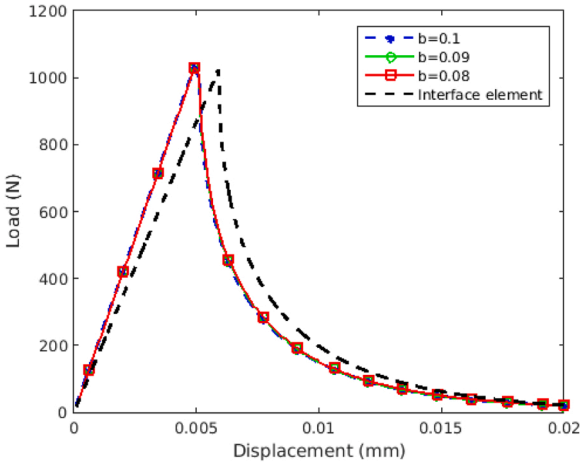

Fig. 20. Effect of length scaling factor with PFM-model2 using exponential softening law (h = 0.02 mm).

due to large damage gradient at the time of decohesion or in other words the slope of the softening curve suddenly changes at the instant of full decohesion. Therefore a fine mesh is required to fully resolve these regions of full decohesion to capture a sudden transition from unbroken to a fully broken state. A similar mesh size effect is also observed for length scaling parameter $b = 0.08mm$.

It is to note here, that due to uniform stress distribution all points within a specimen has equal chances of damage initiation after the stresses reaches the tensile strength. However, the crack initiated near the mid-height of the specimen in all the numerical tests performed above. The non-uniqueness of crack location due to uniform stress distribution is somehow removed due to numerical errors or non-uniform mesh discretization. Consequently, the crack predicted by the phase field model is slightly inclined for some cases which justifies slight variation of phase field results compared to interface element results. In case of interface element analysis, the crack path is defined a priori and is straight.

4.2.2. *Effect of length scaling factor b*

Figure 18 shows the results of analysis for two mesh sizes, i.e. h = 0.02 mm and h = 0.004 mm. It is clear from the Fig. 18 that for larger values of b which gives higher b/h ratio, the results are insensitive to the parameter b. For smaller b/h ratios the numerical results deviate from the reference solution. A very large deviation of the numerical result with b = 0.02 mm is due to the fact that an inclined crack is predicted instead of a straight horizontal crack as shown in Fig. 19. It is therefore concluded that a larger value of b/h with a finer mesh gives good results. Table 4 compares the peak load predicted by the phase field method with interface element analysis. The difference in peak load with respect to the interface element analysis is around 1%. Moreover, the results are insensitive to mesh size.

4.2.3. *Effect of type of softening curve*

To study the effect of type of softening law on length scaling factor b, the analysis is performed considering an exponential softening law. For comparison, interface element analysis is also performed using exponential softening law. Interface element analysis is performed with a dummy stiffness $k_m = 1e6$ N/mm. Fig. 20 shows the analysis results. It is evident from the figure that the analysis results are insensitive to the parameter b. The different analysis results are also in good agreement with each other near the point of full decohesion in contrast to the analysis with linear softening behavior, Fig. 18. This is due to the gradually degrading nature of exponential softening law compared to the linear softening. In case of linear softening the slope of the degrading curve suddenly changes to zero near point of full decohesion.

Figure 20 also compares the analysis results with the interface element model. It is observed that a lower initial stiffness is predicted

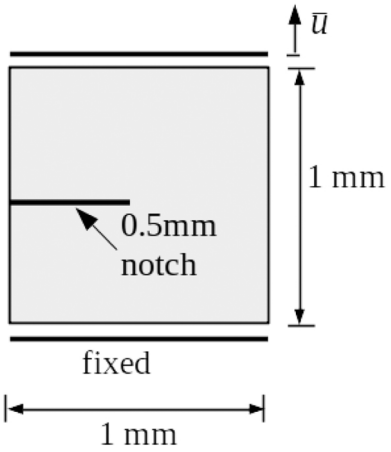

Fig. 21. Geometry and boundary conditions for the uniaxial loaded notched plate.

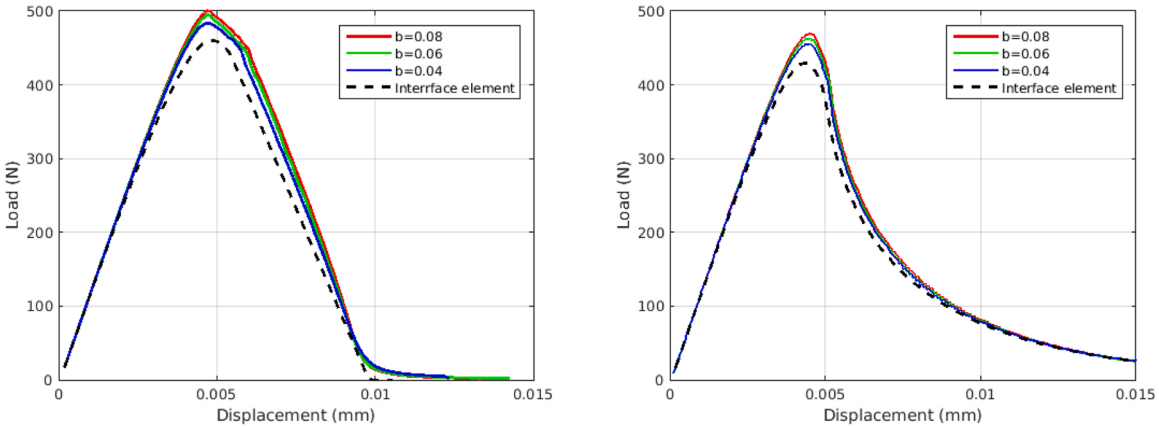

Fig. 22. Load-Displacement curves for the square plate with an edge crack, left: analysis results with linear softening, right: analysis results with exponential softening (a) h = 0.004 mm, b/h = 20,15 and 10; (b) h = 0.004 mm, b/h = 20, 15 and 10.

by the interface model. To remedy this problem interface element analysis is then performed with a higher value of dummy stiffness k_m but the analysis results did not converge for values of k_m larger than 1e6N/mm.

4.3. Uniaxial loaded square plate with an edge crack

In this section performance of the phase filed model (PFM-model2) under non-uniform stress distribution will be studied. In order to incorporate a non-uniform stress distribution a notch is inserted in the middle of the specimen as shown in Fig. 21. Presence of a notch also enforces the crack to initiate at the notch tip and therefore removes the non-uniqueness of crack initiation point as observed in the previous example. The analysis is performed with modulus of elasticity $E = 210$ GPa, Poisson's ratio $\nu = 0$, tensile strength $f_t = 820$ MPa and fracture toughness $G_f = 6$ N/mm. Note that, the fracture material properties are taken different from previous section in order to avoid issues related to dummy stiffness (k_m) in interface element model. To select a value of dummy stiffness, a sensitivity analysis is first performed and it was found that $k_m = 1e8$ N/mm and $k_m = 1e10$ N/mm give similar results. Therefore, interface element analysis is performed with dummy stiffness $k_m = 1e8$ N/mm.

To investigate the effect of length scaling factor b, the analysis is performed with $b = 0.04$, 0.06, 0.08 mm and to investigate the effect of type of softening law on the response, linear and exponential softening laws are used. The analysis is performed with a mesh consisting of minimum element size h = 0.004 mm. Fig. 22 shows analysis results for linear and exponential softening behaviors. Firstly, comparing the peak loads (Figs. 22a and b), it is observed that under non-uniform stress distribution the phase field, as well as the interface element model gives smaller peak loads when exponential softening law is used. Note, that for the case of uniform stress distribution both softening laws gave similar peak loads, Figs. 18 and 20.

Secondly, the load-displacement curves do not match very well with the interface element results compared to the case of a plate

Table 5
Comparison of peak load and percentage difference w.r.t interface element results.

		Linear softening		Exponential softening	
	b (mm)	Peak load (N)	% difference	Peak load (N)	% difference
Interface element	–	460.0	–	429.0	–
PFM-model2	0.04	483.5	5.1	456.0	6.3
PFM-model2	0.06	494.7	7.5	463.0	7.9
PFM-model2	0.08	500.4	8.8	470.0	9.6

subjected to a uniform stress state, Fig. 18. Table 5 compares the peak load predicted by the phase field analysis and interface element analysis. The difference in all cases is less than 10%. It can be concluded, that the phase field model may reproduce interface element results for bodies subjected to uni-axial stress states but under generic multi-axial stress field the results of the phase field and interface element models are different. This is due to inherent differences in defining a material behavior in the two models. Phase field model uses a single constitutive law to define the material behavior over the whole body whereas interface element model uses different constitutive laws for the sharp interface and the bulk material.

Thirdly, the results for different length scaling factors show slight variations in the predicted peak load which necessitate a need for a finer mesh to capture a damage gradient at the time of damage initiation. Moreover, near the point of full decohesion the analysis results with exponential softening are in good agreement with the interface element results due to the fact that damage is gradually decreasing. On the other hand, analysis result using linear softening does not show sharp change in slope near point of full decohesion which requires a finer mesh to resolve the sharp damage gradient. Note, that the same mesh size, h = 0.004 mm, was sufficient enough to capture the decohesion portion of the load-displacement curve in case of uni-axially loaded member, Fig. 18. This indicates that to capture sharp damage gradients for a generic multi-axial stress state a finer mesh is required.

5. Discussion and Conclusions

This section initiates by first presenting a summary of the numerical results followed by general conclusions and key findings of the paper. The paper presented a comparative study among quasi-brittle PFM and brittle PFM, and the interface element model. It was the aim of the paper to determine suitable phase field model functions and model parameters for the simulation of damage in asphalt mixtures. Additionally, the paper also discussed effects of different types of softening laws used within the framework of phase field method. The conclusions drawn hereafter are helpful in appropriate selection of characteristics functions (crack geometric and degradation functions, softening laws) and model parameters for future studies using phase field method.

5.1. Summary of the numerical results

Summary of the important points from the numerical results are given below .

- PFM-model1 and PFM-model2 both are able to simulate initial high stiffness (pre-peak) response of the asphalt mixture, whereas in the case of interface element model the initial pre-peak response depends upon initial stiffness of the chosen interface cohesive constitutive law.
- PFM-model1 is not able to simulate the post-peak response of asphalt mixture. As observed, in PFM-model1 peak stress is dependent upon the length scale factor b and in the limit $b \longrightarrow 0$ peak stress goes to infinity. This is representative of the brittle fracture behavior according to Griffith's theory. On the other hand, PFM-model2 considers the peak stress f_t as an intrinsic material property and independent of the length scaling factor b. Furthermore, any type of softening behavior can be reproduced by calibrating the parameters a_1, a_2 and a_3 for the given softening law. This feature allows the PFM-model2 to simulate quasi-brittle behavior of materials.
- PFM-model1 predicted damage values over the complete domain of the beam even in regions far away from the notch. which is due to the infinite width of the localization band. Whereas, the damaged zone in PFM-model2 is of finite size. The finiteness of the localization band is a useful property and allows the model to be applied to a reduced area of the domain.Therefore, PFM-model2 is more suitable to simulate response of asphalt mixture compared to PFM-model1.
- Both linear and exponential softening curves are suitable to simulate damage in asphalt mixtures. The model parameters f_t and G_f can be calibrated with the experimental results to simulate material behavior.
- Linear softening model gives a large peak load and a faster growth of damaged zone. This is due to the fact that in case of exponential softening model, initial rapid decrease in stiffness causes a reduction in the peak load.
- The calibrated material parameters for the phase field model (PFM-model2) are different from the interface element model under multi-axial stress states. This is due to the inherent characteristics of the two models. Therefore, calibrated material properties using interface elements cannot be used in phase field model.
- Mesh refinement plays a key role in obtaining accurate solution. A fine mesh with a larger b, generally gives good results.
- A fine mesh is required to capture the sharp damage gradients specially in case of generic multi-axial stress states. Softening laws defined with smooth curve near point of damage initiation and full decohesion will give good results with a relatively coarse mesh.
- Interface material properties does not seem to influence the selection of b parameter in this study.

5.2. General conclusions and findings

It is concluded from the study that .

- the response of a material is greatly influenced by the choice of degradation function which relates the bulk material with the damage phase field. The rational based degradation function proposed by [25] is more suitable to simulate the response of asphalt concrete, which behaves in a quasi-brittle manner even at low temperatures. Therefore, phase field models similar to [22,27,28,45], are inadequate to simulate damage in asphalt mixtures.
- both type of softening laws, i.e. linear and exponential, can be used to simulate damage in asphalt mixtures. It should be noted here, that as long as the material behavior is brittle or quasi-brittle, the shape of softening law does not have significant effect on the response [46,47]. The effect is more pronounced in case of ductile material behavior and in micro-scale analysis.
- Phase field model is able to predict the material response but a sufficiently fine mesh (b/h = 5 ~ 10) is required to obtain good results. Mesh refinement demand increases if the curve defining the softening law has kinks.
- material parameters f_t and G_f should be calibrated separately for interface element and phase field models.

This paper presented a comparative study based on quasi-static fracture behavior of asphalt mixtures at low temperatures. Time and temperature dependence is not considered in this contribution, which is a subject of future studies.

Novelty Statement

The manuscript discusses numerical and implementation aspects of phase field model (PFM) in the context of fracture in asphalt mixtures at low temperatures. Phase field model removes most of the constraints of the existing continuum damage and interface element models and provides a unified framework for crack nucleation, propagation and crack branching.

Over the years several variants of phase field models are presented in the literature. This paper investigates the suitability of these models for fracture simulation in asphalt mixtures. A comparative study among quasi-brittle PFM and brittle PFM, and the interface element model is presented. It is the aim of the paper to determine suitable phase field model functions and model parameters for the simulation of damage in asphalt mixtures.

In particular, the key contributions of the manuscript are as follows:

- The paper critically investigates key ingredients of the phase field model and determines the optimal characteristic functions and model parameters for accurate numerical simulation of low temperature fracture in asphalt mixtures.
- A comparative study between phase field method and interface element method is presented and differences in terms of model parameters and analysis results are discussed.
- The effect of type softening laws used within the framework of phase field method combined with cohesive zone model is also investigated.

The conclusions drawn in the paper are helpful in appropriate selection of characteristics functions (crack geometric and degradation functions, softening laws) and model parameters for future studies using phase field method.

The current research work provides relevant and important information on the implementation/numerical aspects of phase field model for damage modeling in asphalt mixtures, therefore, the work will be of interest to many researchers and scientists who are involved in analyzing and studying damage mechanics of asphalt mixtures and failure of pavements.

Declaration of Competing Interest

The authors declare that they have no known competing financial interests or personal relationships that could have appeared to influence the work reported in this paper.

Data Availability

Data will be made available on request.

Appendix A. Pseudo codes

Pseudo codes of the implemented phase field and interface element models are given in the algorithmic boxes 1 and 2, respectively.

Algorithm 1. Algorithm of a finite element code with phase field model.

Require: Given the displacement $\mathbf{a}_n^u$, damage phase field a_n^d and H_n at time t_n, find $\left(\mathbf{a}_{n+1}^u, a_{n+1}^d, H_{n+1}\right)$ at time t_{n+1}

for each loading step `n+1` **do**

  Initialization: Set $\left(\mathbf{a}_n^{u(0)}, a_n^{d(0)}, H_n^{(0)}\right)$ equals to $\left(\mathbf{a}_n^u, a_n^d, H_n\right)$ and j=1

  while Not converged **do**

    Compute damage degradation function: $\omega := \omega\left(a_{n+1}^{d(j-1)}\right)$ and $\omega' := \omega'\left(a_{n+1}^{d(j-1)}\right)$

    Calculate Cauchy stress: $\boldsymbol{\sigma}_{n+1}^{(j-1)}\left(\mathbf{a}_{n+1}^{u(j-1)}, a_{n+1}^{d(j-1)}\right)$

    Update history variable: $\bar{Y}_{n+1} = \max\left(\frac{f_t^2}{2E_o}, \frac{\left(\sigma_{1(n+1)}^{(j-1)}\right)^2}{2E_o}\right)$

$$H_{n+1} = \max\left(H_n, \bar{Y}_{n+1}\right)$$

    Solve equilibrium equations to compute nodal displacement and phase field variables $\left(\mathbf{a}_{n+1}^{u(j)}, a_{n+1}^{d(j)}\right)$

$$\mathbf{R}^u\left(\mathbf{a}_{n+1}^{u(j)}\right) = \int_\Omega (\mathbf{N}^u)^T \bar{\mathbf{b}}\, \mathrm{dV} + \int_{\partial\Omega_t} (\mathbf{N}^u)^T \bar{\mathbf{t}}\, \mathrm{dA} - \int_\Omega (\mathbf{B}^u)^T \boldsymbol{\sigma}_{n+1}^{(j-1)}\, \mathrm{dV} = \mathbf{0}$$

$$\mathbf{R}^d\left(a_{n+1}^{d(j)}\right) = -\int_\Omega (\mathbf{N}^d)^T \left(\omega' H + \frac{G_f}{c_o b}\alpha'\right)\, \mathrm{dV} - \int_\Omega (\mathbf{B}^d)^T \left(\frac{2b}{c_o} G_f \nabla d\right)\, \mathrm{dV} = \mathbf{0}$$

    Set j = j+1

  end while

  Update variables: $\left(\mathbf{a}_n^u, a_n^d, H_n\right)$ equals to $\left(\mathbf{a}_{n+1}^{u(j)}, a_{n+1}^{d(j)}, H_{n+1}\right)$

end for

Algorithm 2. Algorithm of a finite element code with interface element model.

Require: : Given the displacement $\mathbf{a}_n^u$ and damage history d_n at time t_n, find $\left(\mathbf{a}_{n+1}^u, d_{n+1}\right)$ at time t_{n+1}

1: **for** each loading step `n+1` **do**

2: **Initialization:** Set $\left(\mathbf{a}_n^{u(0)}, d_n^{(0)}\right)$ equals to $(\mathbf{a}_n^u, d_n)$ and j=1

3: **while** Not converged **do**

4: Calculate Cauchy stress: $\boldsymbol{\sigma}_{n+1}^{(j-1)}\left(\mathbf{a}_{n+1}^{u(j-1)}\right)$

5: Update damage history variable: $d_{n+1}^{j-1}\left([\![u]\!]_{n+1}^{j-1}\right)$

6: Calculate interface tractions: $\mathbf{t}_{c\,n+1}^{j-1}\left([\![u]\!]_{n+1}^{j-1}, d_{n+1}^{j-1}\right)$

7: Solve equilibrium equations to get nodal displacements $\left(\mathbf{a}_{n+1}^{u(j)}\right)$

$$\mathbf{R}^u\left(\mathbf{a}_{n+1}^{u(j)}\right) = \int_\Omega (\mathbf{N}^u)^T \bar{\mathbf{b}}\ \mathrm{dV} + \int_{\partial\Omega_t} (\mathbf{N}^u)^T \bar{\mathbf{t}}\ \mathrm{dA} - \int_\Omega (\mathbf{B}^u)^T \boldsymbol{\sigma}_o\ \mathrm{dV} + \int_{\partial\Omega_c} (\mathbf{N}^*)^T \mathbf{t}_c\ \mathrm{dA} = \mathbf{0}$$

8: Set j = j+1

9: **end while**

10: Update variables: $(\mathbf{a}_n^u, d_n)$ equals to $\left(\mathbf{a}_{n+1}^{u(j)}, d_{n+1}\right)$

11: **end for**

References

[1] J.B. Soares, F.A. C. de Freitas, D.H. Allen, Crack modeling of asphaltic mixtures considering heterogeneity of the material, In Transportation Research Record: Journal of the Transportation Research Board, No. 1832, (2003)113–120.Transportation Research Board of the National Academies, Washington, D.C.
[2] V. Tavergaard, Effect of fiber debonding in a whisker-reinforced metal, Mater. Sci. Eng. A. 125 (2) (1990) 203–213.
[3] S.H. Song, G.H. Paulino, W.G. Buttlar, Simulation of crack propagation in asphalt concrete using an intrinsic cohesive zone model, ASCE 132 (11) (2006) 1215–1223.
[4] X.P. Xu, A. Needleman, Numerical simulation of fast crack growth in brittle solids, J. Mech. Phys. Solids 42 (9) (1994) 1397–1434.
[5] H. Kim, W.G. Buttlar, Discrete fracture modeling of asphalt concrete, Int. J. Solids Struct. 46 (2009) 2593–2604.
[6] H. Kim, M.P. Wagnor, W.G. Buttlar, Micromechanical fracture modeling of asphalt concrete usiing a single-edge notched beam test, Mater. Struct. 42 (2009) 677–689.
[7] Y.-R. Kim, F.T.S. Aragao, Microstructure modeling of rate-dependent fracture behavior in bituminous paving mixtures, Finite Elem. Anal. Des. 63 (2013) 23–32.
[8] S. Caro, E. Masad, A. Bhasin, D. Little, Micromechanical modeling of the influence of material properties on moisture-induced damage in asphalt mixtures, Constr. Build. Mater. 24 (2010) 1184–1192.
[9] H. Ban, Y.-R. Kim, S.-K. Rhee, Computational microstructure modeling to estimate progressive moisture damage behavior of asphaltic paving mixtures, Int. J. Numer. Anal. Methods Geomech. 37 (13) (2012) 2005–2020.
[10] E.V. Dave, S. Song, W.G. Buttlar, G.H. Paulino, Reflective and thermal cracking modeling of asphalt concrete overlays, in: Loizos, Al-Qad Scarpas (Eds.), Adv. Charac. Pavement Soil Eng. Mater., Taylor & Francis Group London, 2007.
[11] H. Ban, S. Im, Y.-R. Kim, J.S. Jung, Laboratory tests and finite element simulations to model thermally induced reflective cracking of composite pavements, Int. J. Pavement Eng. 18 (6) (2017) 1–11.
[12] T. You, Y.-R. Kim, K.Z. Rami, D.N. Little, Multiscale modeling of asphaltic pavements: Comparison with field performance and parametric analysis of design variables, J. Transp. Eng. B: Pavements 144 (2) (2018), 0408012.
[13] Z.P. Bazant, B. Oh, Crack band theory for fracture of concrete, Mater. Struct. 16 (1983) 155–177.
[14] R. Peerlings, R. de Borst, W. Brekelmans, J. de Vree, Gradient-enhanced damage for quasi-brittle materials, Int. J. Numer. Methods Eng. 3 (1996) 331–3404.
[15] G. Zeng, X. Yang, A. Yin, F. Bai, Simulation of damage evolution and crack propagation in three-point bending pre-cracked asphalt mixture beam, Constr. Build. Mater. 55 (2014) 323–332.
[16] R.R. Rastegar, E.V. Dave, J.S. Daniel, Fatigue and thermal cracking analysis of asphalt mixtures using continuum-damage and cohesive-zone models, J. Transp. Eng. B: Pavements 144 (4) (2018).
[17] C. Kuhn, R. Muller, Phase field simulation of thermomechanical fracture, Proc. Appl. Math. Mech. 9 (2009) 191–192.
[18] Z.A. Wilson, C.M. Landis, Phase-field modeling of hydraulic fracture, J. Mech. Phys. Solids 96 (2016) 264–290.
[19] J.-Y. Wu, T.K. Mandal, V.P. Nguyen, A phase-field regularized cohesive zone model for hydrogen assisted cracking, Comput. Methods Appl. Mech. Eng. 358 (2020), 112614.
[20] G. Francfort, J. Marigo, Revisiting brittle fracture as an energy minimization problem, J. Mech. Phys. Solids 46 (8) (1998) 1319–1342.
[21] B. Bourdin, G.A. Francfort, J.J. Marigo, Numerical experiments in revisited brittle fracture, J. Mech. Phys. Solids 48 (4) (2000) 797–826.
[22] C. Miehe, F. Welschinger, M. Hofacker, Thermodynamically consistent phase-field models of fracture:variational principles and multi-field fe implementations, Int. J. Numer. Methods Eng. 83 (2010) 1273–1311.
[23] C. Miehe, M. Hofacker, F. Welschinger, A phase field model for rate-independent crack propagation: robust algorithmic implementation based on operator splits, Comput. Methods Appl. Mech. Eng. 199 (45–48) (2010) 2765–2778.
[24] C.V. Verhoosel, R. de Borst, A phase-field model for cohesive fracture, Int. J. Numer. Methods Eng. 96 (2013) 43–62.
[25] J.Y. Wu, A unified phase-field theory for the mechanicsof damage and quasi-brittle failure, J. Mech. Phys. Solids 103 (2017) 72–99.
[26] C. Kuhn, R. Muller, A continuum phase field model for fracture, Eng. Fract. Mech. 77 (2010) 3625–3634.
[27] C. Kuhn, A. Schluter, R. Muller, On degradation functions in phase field fracture models, Comput. Mater. Sci. 108 (2015) 374–384.
[28] Y. Hou, Computational analysis of asphalt binder based on pahse field method, 2014.
[29] Y. Hou, L. Wang, P. Yue, W. Sun, Fracture failure in crack interaction of asphalt by using a phase field approach, Mater. Struct. 48 (2015) 2997–3008.
[30] A. Ahmed, R. Khan, A phase field model for damage in asphlat concrete, Int. J. Pavement Eng. (2021) 1–13, https://doi.org/10.1080/10298436.2021.1942871.
[31] Y. Hou, L. Wang, P. Yue, T. Pauli, W. Sun, Modeling mode i cracking failure in asphalt binder by using a non-conserved phase field model, 4, ASCE, 2014.
[32] P. Yue, J.J. Feng, C. Liu, J. Shen, A diffuse-interface method for simulaing two-phase flows of complex fluid, J. Fluid Mech. 515 (2004) 293–317.
[33] B. Bourdin, C.J. Larsen, C.L. Richardson, A time-discrete model for dynamic fracture based on crack regularization, Int. J. Fract. 168 (2011) 133–143.
[34] V.I. Levitas, H. Jafarzadeh, G.H. Farrahi, M. Javanbakht, Thermodynamically consistent and scale-dependent phase field approach for crack propagation allowing for surface stresses, Int. J. Plast. 111 (2018) 1–35.
[35] G.H. Farrahi, M. Javanbakht, H. Jafarzadeh, On the phase field modeling of crack growth and analytical treatment on the parameters, Contin. Mech. Thermodyn. 32 (2020) 589–606.
[36] K. Pham, H. Amor, J.-J. Marigo, C. Maurini, Gradient damage models and their use to approximate brittle fracture, Int. J. Damage Mech. 20 (2011) 618–652.
[37] H. Amor, J.J. Marigo, C. Maurini, Regularized formulation of the variational brittle fracture with unilateral contact: Numerical experiments, J. Mech. Phys. Solids 57 (8) (2009) 1209–1229.
[38] P. Farrell, C. Maurini, Linear and nonlinear solvers for variational phase-field models of brittle fracture, Int. J. Numer. Methods Eng. 109 (2017) 648–667.
[39] J.Y. Wu, Robust numerical implementation of non-standard phase-field damage models for failure in solids, Comput. Methods Appl. Mech. Eng. 340 (2018) 767–797.
[40] A. Turon, P.P. Camanho, J. Costa, C.G. Davila, A damage model for the simulation of delamination in advanced composites under variable-mode loading, Mech. Mater. 38 (11) (2006) 1072–1089.
[41] M.P. Wagnor, W.G. Buttlar, G.H. Paulino, Development of a single-edge notched beam test for asphalt concrete mixtures, J. Test. Eval. 33 (2005).
[42] H. Cornelissen, D. Hordijk, H. Reingardt, Experimental determination of crack softening characteristics of normalweight and lightweight concrete, HERON 32 (2) (1986) 45–56.
[43] E.V. Dave, B. Behnia, Cohesive zone fracture modelling of asphalt pavements with applications to design of high-performance asphalt overlays, Int. J. Pavement Eng. 19 (2018) 319–337.
[44] G. Molnar, A. Gravouil, 2d and 3d abaqus implementation of a robust staggered phase-field solution for modeling brittle fracture, Finite Elem. Anal. Des. 130 (2017) 27–38.
[45] Y. Hou, W. Sun, Y. Huang, M.R. Ayatullahi, L. Wang, J. Zhang, Diffuse interface model to investigate the asphalt concrete cracking subjected to shear loading at low temperature, ASCE 31 (2) (2016).
[46] R. de Borst, Numerical aspects of cohesive-zone models, Eng. Fract. Mech. 70 (14) (2003) 1743–1757.
[47] J. Zhang, J. Wang, Z. Yuan, H. Jia, Effect of the cohesive law shape on the modelling of adhesive joints bonded with brittle and ductile adhesives, Int. J. Adhes. Adhes. 85 (2018) 37–43.